Chemical Geology 577 (2021) 120295

Contents lists available at ScienceDirect

Chemical Geology

journal homepage: www.elsevier.com/locate/chemgeo

Invited Research Article

Groundwater controls REE mineralisation in the regolith of South China

Jian Huang [a,b,c], Hongping He [a,b,c,*], Wei Tan [a,b], Xiaoliang Liang [a,b,c], Lingya Ma [a,b], Yuanyuan Wang [a,b,c], Xiaorong Qin [a,b,c], Jianxi Zhu [a,b,c]

[a] CAS Key Laboratory of Mineralogy and Metallogeny/Guangdong Provincial Key Laboratory of Mineral Physics and Materials, Guangzhou Institute of Geochemistry, Chinese Academy of Sciences, Guangzhou 510640, China
[b] CAS Center for Excellence in Deep Earth Science, Guangzhou 510640, China
[c] University of Chinese Academy of Sciences, Beijing 100049, China

ARTICLE INFO

Editor: Dr. Hailiang Dong

Keywords:
Groundwater
Groundwater table
Ion exchangeable REEs
Regolith-hosted REE deposits

ABSTRACT

Regolith-hosted rare earth element (REE) deposits in South China have attracted widespread attention due to their crucial applications in technology and renewable energy solutions. However, the factors that control the formation of REE deposits in regolith remain poorly understood. Groundwater plays important roles in the physico-chemical environments of regolith. In particular, groundwater in the vadose and saturated zones, which are divided by the groundwater table, has distinct hydrological and physico-chemical properties and is likely to impose different effects on activation, migration, and enrichment of REEs in regolith. Our comprehensive geochemical and mineralogical investigations of the Renju REE deposits in South China suggest that the abrupt change of cerium (Ce) anomaly values, the occurrence of Fe-REE oxide colloids, and the prominent variation of goethite and hematite contents can be used as effective indicators for the groundwater table in the regolith. The distribution and geochemical behaviour of REEs reveal that the highly permeable vadose zone facilitates the downward migration of REEs liberated via dissolution of REE-bearing minerals by seepage water, whereas the relatively stable and high-pH saturated zone facilitates the adsorption of REE ions by kaolinite and halloysite. The long-term eluviation–illuviation processes led to the continuous accumulation of REEs in the saturated zone and, ultimately, the formation of lenticular-shaped REE ore bodies. The present study highlights the distinctive roles of groundwater in the vadose and saturated zones with regard to the activation, migration, and enrichment of REEs in the regolith of South China.

1. Introduction

Regolith-hosted rare earth element (REE) deposits in South China supply approximately 20% of the global REE production and more than 90% of the global heavy rare earth element (HREE) production (Sanematsu and Watanabe, 2016; Riesgo García et al., 2017). Granites and felsic volcanic rocks in South China were subjected to intensive chemical weathering and thus formed regolith with thicknesses up to tens of meters under subtropical monsoon climate conditions (Sanematsu and Watanabe, 2016; Fu et al., 2019). During regolith formation, REEs released by REE-bearing minerals decomposition leach downwards and are subsequently adsorbed on and accumulated by clay minerals and Fe-(hydr)oxides in the lower part of the regolith (Duzgoren-Aydin and Aydin, 2009; Braun et al., 2018; Borst et al., 2020; Li and Zhou, 2020).

Many factors have been suggested to influence REE mineralisation in regolith, such as the properties of REE-bearing minerals (Fu et al., 2019; Li et al., 2019) and supergene minerals (Yu et al., 2017; Li and Zhou, 2020), the weathering environments (e.g., pH and Eh) (Tang and Johannesson, 2010; Berger et al., 2014; Bray et al., 2015), and regional exogenetic conditions (e.g., microbial activity, landforms, and water) (Taunton et al., 2000; Aubert et al., 2001; Rasmussen et al., 2011; Li et al., 2020). Among these factors, water can impose multiple effects on the physico-chemical environments of regolith. For example, soil drying increases the air-filled soil pore volume, whereas soil wetting inhibits oxygenation and lowers redox potentials (Holden and Fierer, 2005; Zhukov and Bogatyrev, 2012; Arora et al., 2019). Water also provides a driving force for the migration and enrichment of REEs in regolith (King and Pett-Ridge, 2018; Alakangas et al., 2020; Wallrich et al., 2020). For example, laterally flowing groundwater was shown to transport HREEs along hillslopes, leading to their accumulation in the lower part of the

* Corresponding author at: CAS Key Laboratory of Mineralogy and Metallogeny/Guangdong Provincial Key Laboratory of Mineral Physics and Materials, Guangzhou Institute of Geochemistry, Chinese Academy of Sciences, Guangzhou 510640, China.
E-mail address: hehp@gig.ac.cn (H. He).

https://doi.org/10.1016/j.chemgeo.2021.120295
Received 25 February 2021; Received in revised form 25 April 2021; Accepted 27 April 2021
Available online 29 April 2021

footslope profile in the Bankeng light rare earth element (LREE) deposit (Li et al., 2020).

The groundwater table divides regolith into two zones with distinct hydrological conditions. The vadose zone consists of unsaturated porous media and unweathered minerals and extends from the soil surface to the groundwater table (Holden and Fierer, 2005; Arora et al., 2019). Pore spaces in the vadose zone are generally air-filled and only fill with water when rainfall percolates, followed by rapid drainage and gradual drying (Holden and Fierer, 2005). In contrast, the saturated zone below the groundwater table is an unconfined aquifer that can remain stable over timescales of years (Niswonger et al., 2006; Gleeson et al., 2016; Arora et al., 2019) and acts as an important geochemical barrier, representing the significant contrast between the hydrologic and redox environments in regolith (Zhukov and Bogatyrev, 2012; Öhlander et al., 2014; Navarre-Sitchler et al., 2015). Moreover, the distinct infiltration rates in the vadose zone and saturated zone also pose different underlying effects on illuviation–eluviation dynamics and water–mineral reactions (Zhukov and Bogatyrev, 2012; Öhlander et al., 2014). However, the specific effects of water in these zones on the activation, migration, and enrichment of REEs in regolith remain poorly understood.

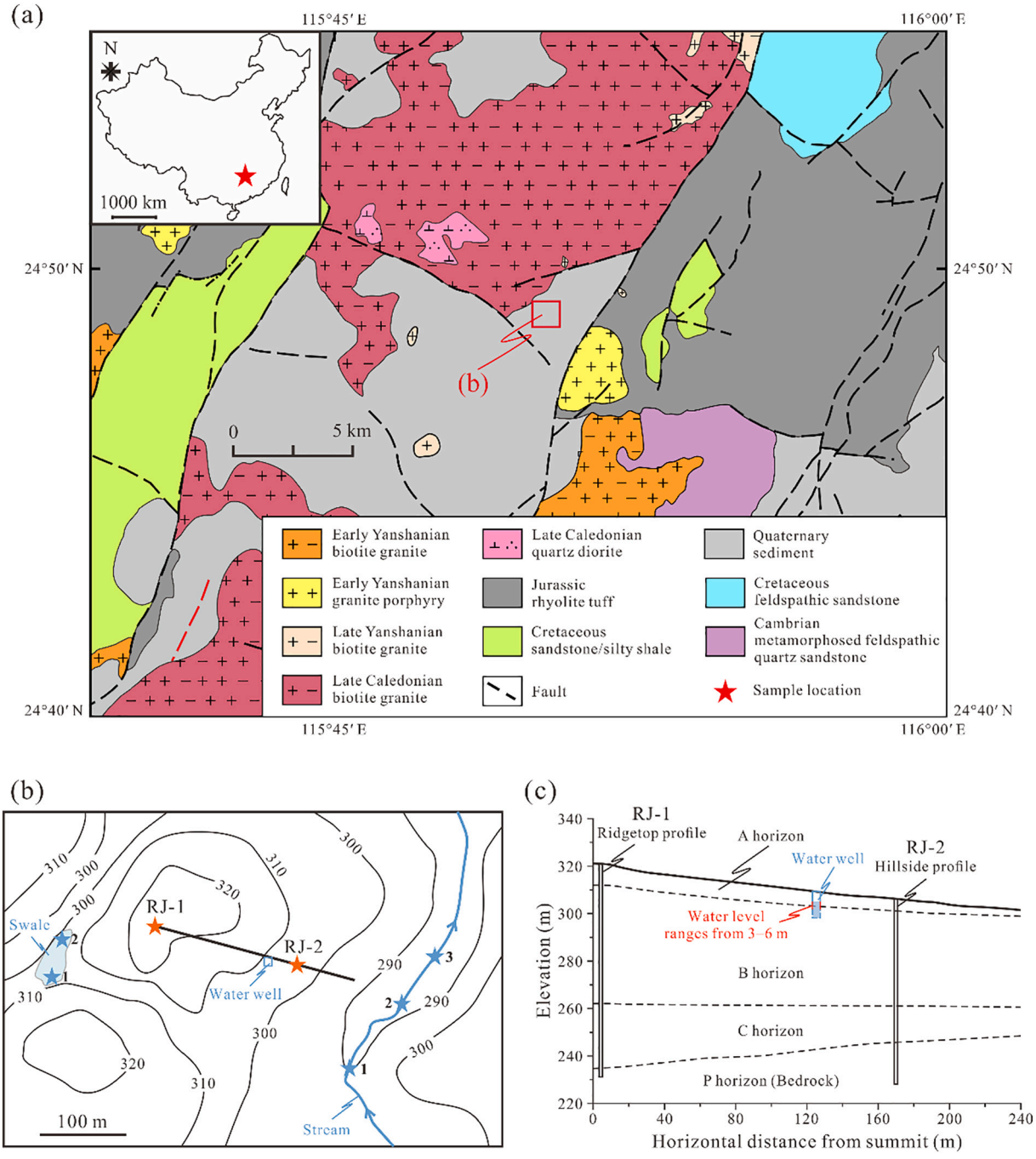

Fig. 1. (a) Location and simplified geologic map of the Renju rare earth element (REE) deposit (after Regional Geological Survey Team of Jiangxi Geological Bureau, 1976). The red star indicates the deposit. (b) Simplified topographic contour map (unit: m) and (c) a representative longitudinal section of the study area. The locations of the soil profiles and water well discussed in the text are marked on the section. The orange and blue stars indicate the locations of the weathering profiles and groundwater sample collection, respectively. (For interpretation of the references to colour in this figure legend, the reader is referred to the web version of this article.)

In this study, we obtained detailed mineralogical and geochemical data from regolith profiles along a hillslope in the Renju regolith-hosted REE deposit. We firstly propose several effective mineralogical and geochemical proxies for locating the groundwater table in regolith. We also investigated mineral phase transitions, element migration and enrichment behaviours, and REE speciation to elucidate the influence of groundwater on REE mineralisation in regolith-hosted REE deposits. The results highlight the distinct roles of groundwater in the vadose zone and saturated zone with regard to the activation, migration, and enrichment of REEs in the regolith of South China.

2. Geological background

The Renju REE deposit in the northeastern Guangdong Province currently has a total rare earth oxides (REO) resource of 20,467 tons with a grade of 0.153–0.197 wt% REOs (Chen and Yu, 1994; Wang and Xu, 2016). Biotite granite, granite porphyry, and quartz diorite formed by multistage magmatic activities are distributed in the Renju mining area (Fig. 1a). The igneous rocks intruded in the Cambrian sediments are commonly overlaid by small quantities of Quaternary and Cretaceous sediments and Yanshanian rhyolite tuff (Fig. 1a). Caledonian and Yanshan fold structures and N-*E*- and N-W-trending faults are well developed in the Renju mining area (Chen and Yu, 1994, 1995), which is situated on early Yanshanian granitoid plutons with outcrops covering 29.3 km^2 (Wang and Xu, 2016).

The Renju REE deposit is located in a region with moderately undulating landforms. The elevation in this region varies from approximately 250 to 350 m above sea level, and the slope gradient is generally <25° (Fig. 1b). This region is subjected to an East Asian monsoon climate with an annual rainfall of 1500–2000 mm and average temperature of ~25 °C (Yang et al., 2019). A stream is present in the valley neighbouring the mining area (Fig. 1b). Seasonal inter-hill swales occur due to sufficient rainfall from April to May. Field investigations revealed that the thickness of the regolith in the Renju REE deposit generally ranges from a few to several tens of meters, and gradually thins toward the foothills (Fig. 1c). The REE ore bodies are distributed as crescent lenses with thicknesses of a few to up to 20 m, which are likely controlled by local landforms (Wang and Xu, 2016).

3. Materials and methods

3.1. Sampling and pretreatment

Drill core samples were collected using a custom-made double-tube drilling system comprising a stainless steel outer tube equipped with a diamond drill bit and an inner PVC tube. Two drill cores representing weathering profiles on the ridge (RJ-1) and hillside (RJ-2) were obtained (Fig. 1). The outermost parts of the drill core samples were scraped off to prevent contamination from the drilling system. Forty-two regolith samples and three rock samples from the RJ-1 profile, and thirty-five regolith samples and three rock samples from the RJ-2 profile were collected. The samples were air dried and ground into powder with particle size of <75 μm for further analyses of the mineral composition, major/trace elements, pH, and REE speciation. Resin-impregnated thin sections of samples collected from different depths of the profiles were prepared for petrographic observations.

Five water samples were collected, including two samples from a swale formed in the rainy season and three samples from a perennial stream (Fig. 1b). As the swale was located above the groundwater table, the swale samples represent water that percolated from laterite in the regolith (Kimberley and Abu-Jaber, 2005; Salve et al., 2012). In contrast, the stream contains regional seepage water and infiltrates the entire regolith (Tóth et al., 2016; Wang et al., 2016), and therefore the water samples are compositionally analogous to the groundwater in the saturated zone. The water samples were stored in Teflon bottles in a refrigerator at temperatures of 0–4 °C prior to analysis.

3.2. Mineral compositions

The mineral compositions of the bedrock and regolith were analysed using a Bruker D8 Advance X-ray diffractometer (XRD) at the Key Laboratory of Mineralogy and Metallogeny of the Guangzhou Institute of Geochemistry, Chinese Academy of Sciences (GIGCAS). The analysis was carried out using Cu Kα radiation at an accelerating voltage of 40 kV and beam current of 40 mA. The scan range (2θ) was from 3° to 80° at a scan speed of 3° min^{-1}. The XRD patterns were analysed using JADE 6.0 software to obtain quantitative mineral composition data (Appendix Tables A.1–A.2). Petrographic observations were conducted using a Hitachi SU8010 scanning electron microscope (SEM) equipped with an energy dispersive X-ray spectrometer (EDS) at an accelerating voltage of 15 kV and beam current of 20 nA. Transmission electron microscope (TEM) images were obtained using an FEI Talos F200S instrument operating at 200 kV.

The Fe-(hydr)oxide phases were analysed using an Analytical Spectral Devices FieldSpec-3 spectrometer equipped with a circle detector (see Supplementary Text 1 for the details of analysis procedure). The results of the visible and near-infrared reflectance spectrometry (VNIR) analyses are presented in Appendix Table A.3.

3.3. Major and trace elements

The major and trace elements of bulk powder samples was analysed by Rigaku ZSX100e X-ray fluorescence spectrometer (XRF) and Thermo Icap Qc inductively coupled plasma-mass spectrometer (ICP-MS), respectively (see Supplementary Text 2 for the details of analysis procedure). The major element analysis results are listed in Appendix Tables A.4–A.5. The results of the trace element analyses are listed in Appendix Tables A.6–A.7.

The water samples were acidified and filtered with a cellulose acetate membrane (pore sizes of 0.45 μm) before analysis. The REE concentrations in the water samples were measured using an ICP-MS at the State Key Laboratory of Isotope Geochemistry, GIGCAS, and the results are shown in Appendix Table A.8.

3.4. Ion-exchangeable REE content

A sequential extraction routine following the method of Fu et al. (2019) and Denys et al. (2021) was used to evaluate the ion-exchangeable REE (iREE) fractions in the regolith samples. The targets of the extraction were assumed to be in the water-soluble fraction (step I) and extracted by purified H_2O (pH = 7 ± 0.2). The ion-exchangeable fraction (step II) was extracted using $MgCl_2$ solution (pH = 7 ± 0.2), the carbonate binding fraction (step III) was extracted using CH_3COONa solution (pH = 5 ± 0.2), the humic acid binding fraction (step IV) was extracted using $Na_4P_2O_7$ solution (pH = 10 ± 0.2), the Fe-(hydr)oxide fraction (step V) was extracted using NH_2OH–HCl solution (pH = 2 ± 0.2), the strong organic binding fraction (step VI) was extracted using H_2O_2 + HNO_3, and finally the residual fraction (step VII) was extracted using HNO_3–HF–$HClO_4$ solution. After each extraction step, the REE concentrations in the collected filtrates were measured using an ICP-MS at the State Key Laboratory of Isotope Geochemistry, GIGCAS. The recovery rates of all seven REE fractions relative to total REE amount ranged between 85% and 105% (Appendix Tables A.9–A.10).

3.5. pH values

Ten grams of each powder sample were fully mixed with 25.0 g of Milli-Q double de-ionised water (18.25 MΩ cm^{-1}) in a capped beaker for 8 h. The pH values of the powder samples were determined by measuring the filtered liquid with a Mettler-Toledo FiveEasy Plus™ pH meter with a precision better than 0.02. The pH values of the regolith samples are listed in Appendix Table A.11. The pH values of the water samples were directly measured using the Mettler-Toledo FiveEasy

Plus™ pH meter.

4. Results

4.1. Characteristics of the Renju regolith profile

The RJ-1 and RJ-2 profiles display similar petrologic sequences, whereas the thickness of each petrologic unit in RJ-1 is generally larger than that in RJ-2. From top down, the regolith profiles can be divided into different horizons based on the weathering intensity, including an A horizon, a B horizon consisting of upper and lower B horizons, a C horizon, and quartz diorite bedrock (P horizon) (Fig. 1c). The two regolith profiles exhibit similar weathering intensity trends, which can be characterised by the chemical index of alteration (CIA; $Al_2O_3/(Al_2O_3 + CaO + Na_2O + K_2O) \times 100$) (Nesbitt and Young, 1982). From the bedrock to the A horizon, the primary rock-forming minerals gradually transform into clay minerals and Fe-(hydr)oxides with increasing CIA (Fig. 2). The pH values gradually increase with increasing depth from 4.27 at the topsoil to 7.25 at the C horizon (Fig. 2).

The A horizon (CIA > 90) is red in colour and is characterised by a loose structure containing a small amount of pores. The A horizon is mainly composed of supergene minerals with some rounded residual quartz grains, whereas primary feldspar and biotite are essentially absent. Kaolinite and halloysite are the main supergene minerals, accounting for 33%–71% of the total content in the A horizon.

The upper B horizon (CIA = 80–90) is mottled red and white in colour, likely due to the heterogeneous distribution of Fe-oxide minerals in the clay mineral aggregates. The clay minerals in this horizon include kaolinite and halloysite, accounting for 26%–71% of the bulk sample, and the abundance exhibits a decreasing trend from top to bottom.

The lower B horizon (CIA = 75–80) is more compact than the upper B horizon and is a mottled brownish-yellow colour. The clay minerals in this layer gradually change from kaolinite/halloysite to smectite/illite, with the content of the latter gradually increasing to 49% from top to bottom.

The C horizon (CIA = 70–75) exhibits a yellow-green colour and contains fragments of the protolith rock. Kaolinite and halloysite gradually disappear in this horizon, and smectite and illite become the dominant supergene minerals, accounting for 4%–50% of the bulk sample (Fig. 2).

4.2. Morphology and phase variations of Fe-oxides

With the dissolution of primary Fe oxide minerals (e.g., magnetite and ilmenite) and Fe-bearing silicate minerals (e.g., biotite and amphibole), the released Fe tends to form goethite and hematite in the regolith

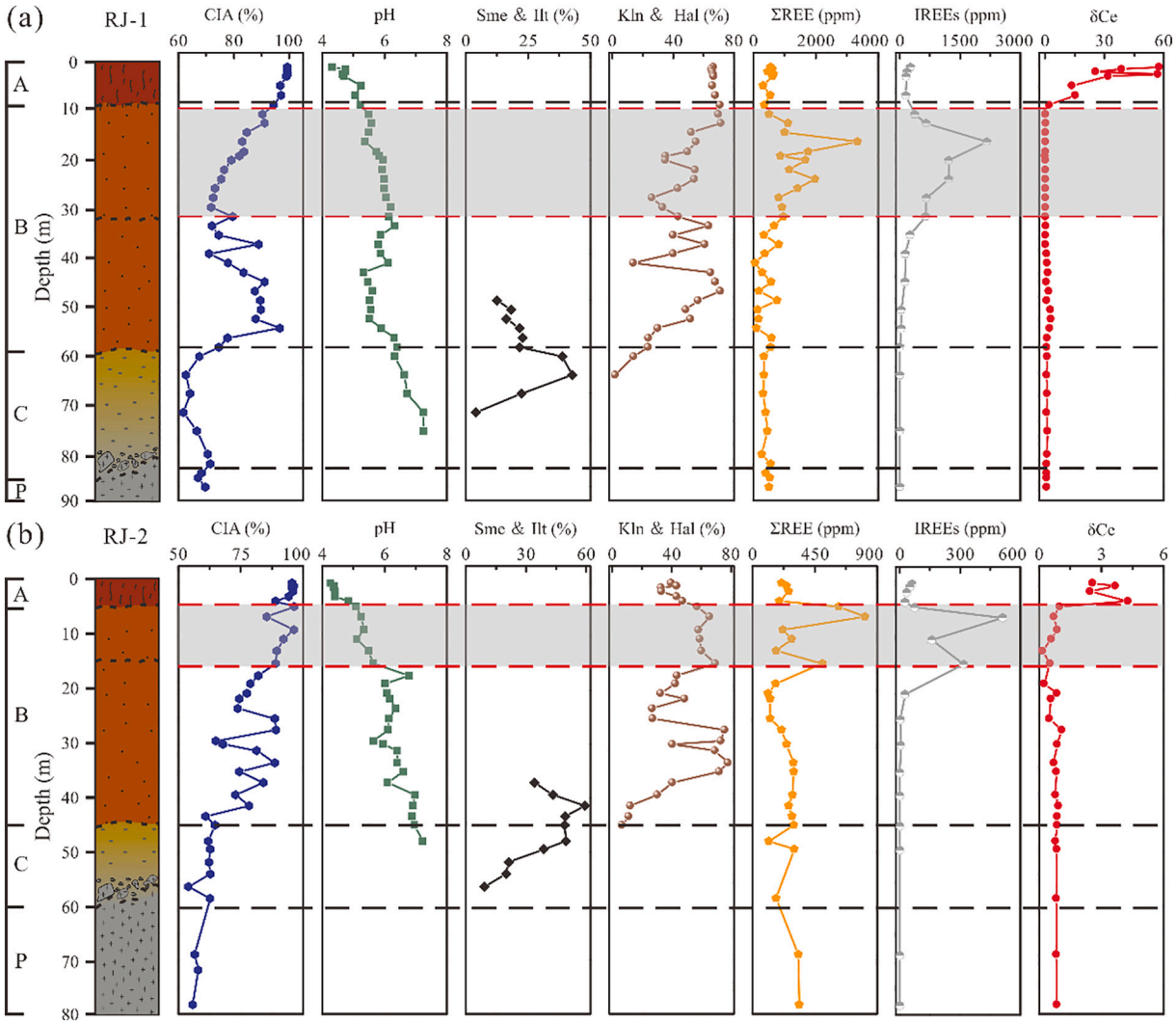

Fig. 2. Weathering horizons and vertical variations in the chemical index of alteration (CIA), pH, smectite/illite, kaolinite/halloysite, total rare earth elements (ΣREE), ion-exchangeable rare earth elements (iREEs), and the Ce anomalies (δCe) in the bulk samples as a function of depth in the (a) RJ-1 and (b) RJ-2 weathering profiles. The shaded area represents the REE fertile zone. $\delta Ce = Ce_N/(La_N \times Pr_N)^{1/2}$, where N is C1-chondrite normalised (McDonough and Sun, 1995).

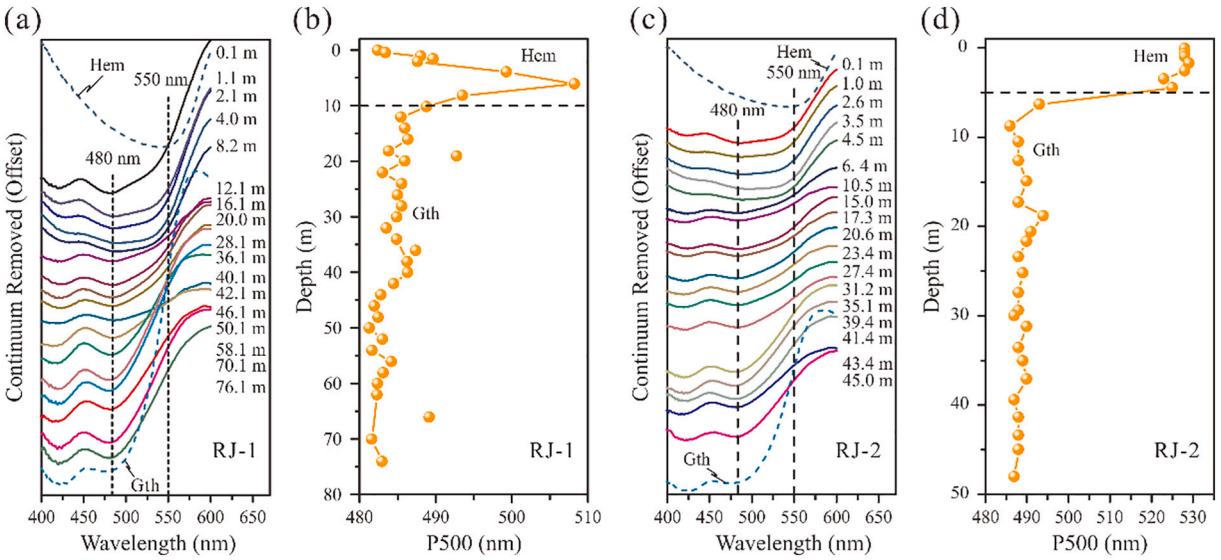

Fig. 3. Visible and short-wave infrared reflectance spectra at the 400–600 nm band and variations in the relative content of Fe-oxides in the (a, b) RJ-1 and (c, d) RJ-2 regolith samples. The characteristic adsorption peaks of hematite (Hem) and goethite (Gth) (P500) are 550 and 480 nm, respectively.

(Fig. 3). The band position of the VNIR spectra near the wavelength of 500 nm (P500) has been regarded as an index to distinguish between hematite and goethite (Cudahy and Ramanaidou, 1997; Zhao et al., 2018). The P500 of hematite generally occurs at ~550 nm, whereas that of goethite occurs at ~480 nm (Cudahy and Ramanaidou, 1997). Interestingly, a boundary marking a significant shift of the characteristic P500 occurs at a depth of ~10 m in the RJ-1 profile and ~ 5 m in the RJ-2 profile (Fig. 3a, c). Above this boundary, the P500 is concentrated at

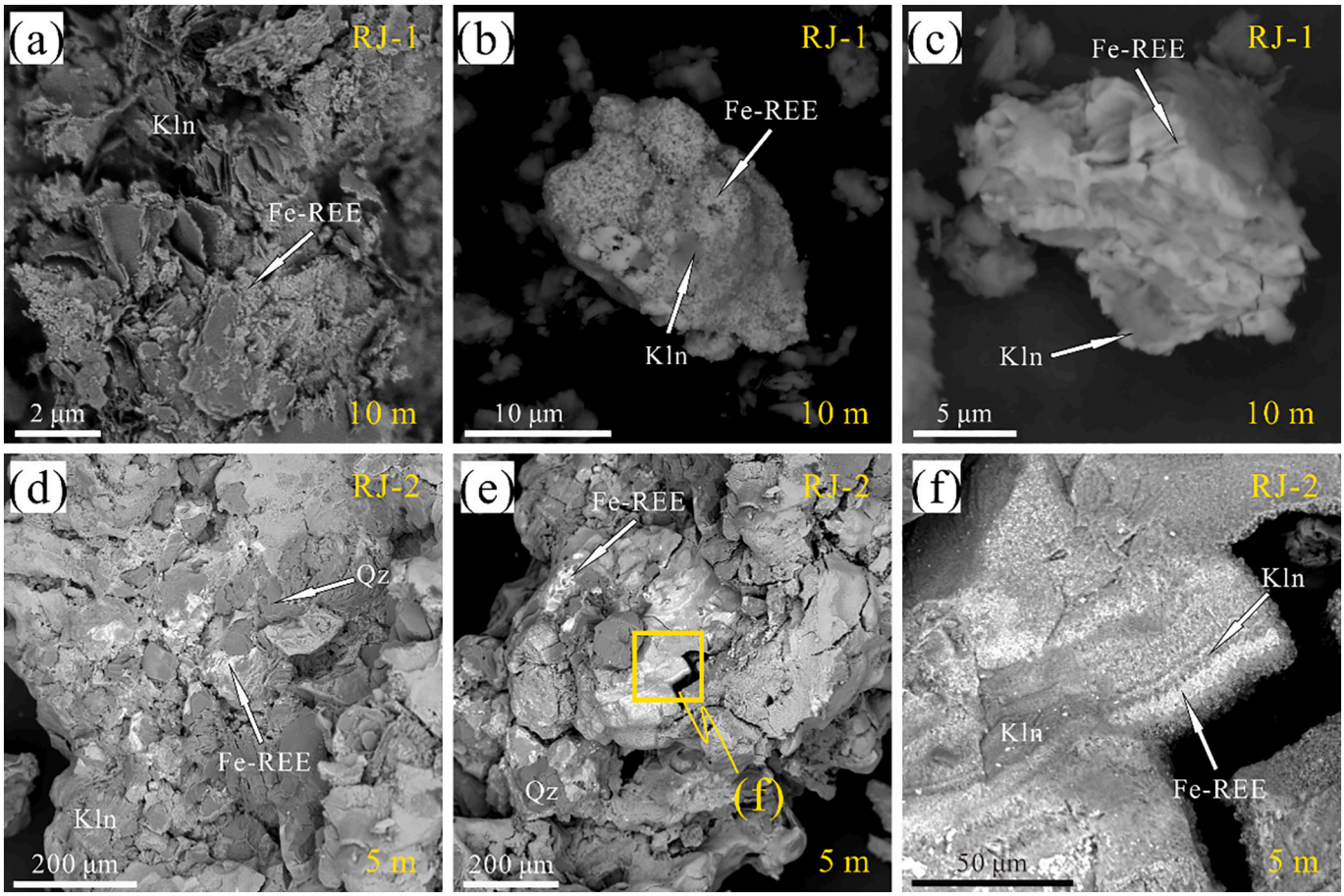

Fig. 4. Scanning electron microscopy backscattered electron images showing the slag and lamellar Fe-oxide colloids in the Renju weathering crust. Slag and lamellar colloids at approximately (a–c) 10-m depth in the RJ-1 regolith and (d–f) 5-m depth in the RJ-2 regolith. Abbreviations: Fe-REE = Fe-rare earth element oxides; Kln = kaolinite; Qz = quartz.

510–530 nm, indicating that hematite is dominant in the Fe-oxides; below the boundary, the P500 shifts toward 480 nm, indicating that goethite becomes the dominant component phase of the Fe-oxides (Fig. 3b, d).

Notably, a number of colloids composed of quartz, clay minerals, and Fe-REE oxides occur at a depth of ~10 m in the RJ-1 profile (Fig. 4a–c) and ~ 5 m in the RJ-2 profile (Fig. 4d–f). During the initial formation of these colloids, lamellar kaolinite gradually blended into an argillaceous adhesive (Fig. 4a), which aggregated with surrounding spherical Fe-REE oxides and refractory quartz grains to form granular (Fig. 4b), massive (Fig. 4c), slag (Fig. 4d), and lamellar colloids (Fig. 4e). The lamellar colloids consist of periodically interlaced kaolinite and Fe-REE oxides (Fig. 4f).

4.3. REE distributions in the regolith profiles

The investigated bedrock of the RJ-1 and RJ-2 profiles contains total REE (ΣREE) concentrations of 496–522 and 333–338 ppm, respectively (Fig. 2), which are higher than the average ΣREE contents (~229 ppm) of granites in South China (Shi et al., 2005). The ΣREE concentrations in the regolith profiles are highly concentrated in the upper B horizon (Fig. 2), which are ~6.6 fold (ΣREE_{max} = 3343 ppm) and ~ 2.4 fold (ΣREE_{max} = 813 ppm) higher than the bedrock in the RJ-1 and RJ-2 regolith profiles, respectively. iREEs are the main resource for exploitation and industrial use. The distributions of iREEs nearly overlap with the ΣREE distributions in the regolith profiles and are significantly enriched in the upper B horizons (Fig. 2). For example, the iREEs in the RJ-1 profile abruptly increase from 148 to 264 ppm in the A horizon to 366–2163 ppm in the upper B horizon, then sharply decrease to <254 ppm in the C horizon (Fig. 2a).

A boundary marking the Ce anomaly also occurs at depths of ~10 m in the RJ-1 profile and ~ 5 m in the RJ-2 profile. The Ce anomalies are all greater than 1 (δCe = 2.11–57.7) above the boundary, indicating positive Ce anomalies, but generally less than 1 (δCe = 0.03–0.99) below the boundary, indicating negative Ce anomalies. Note that, above the boundary, RJ-1 has higher positive Ce anomaly values (δCe = 2.11–57.7) than RJ-2 (δCe = 2.57–4.28) (Fig. 2). Petrographic observations revealed that aggregates of granulate cerianite (5–20 nm) are generally attached to the surfaces of tubular halloysite and laminar kaolinite particles in the A horizons (Fig. 5a, 5b). The HRTEM images show that typical plane distances of 0.31, 0.27, and 0.19 nm are assigned to the (111), (200), and (220) planes of cerianite, respectively (Fig. 5c, 5d).

4.4. Chemical properties of water samples

The pH analyses indicated that the water samples collected from the swale are weakly acidic, with pH values ranging from 5.12 to 6.14 (Appendix Table A.8), which are similar to those of the lower A horizon in the Renju regolith profiles (Fig. 2a). The swale water samples had relatively high REE concentrations (32.4–37.2 ppm). The chondrite-normalised REE patterns revealed that the swale water is enriched in LREEs (LREE/HREE = 1.61–1.65) with a significant negative Ce anomaly (δCe = 0.04) and a slightly negative Eu anomaly (δEu = 0.66) (Fig. 6a). Aside from the Ce anomaly, the REE patterns of the swale water are almost identical to those of the A horizon in the Renju regolith profiles (Fig. 6a).

The water samples collected from the stream had generally neutral pH values (6.59–7.01) similar to those of the lower B horizon in the Renju regolith profiles (Fig. 2b). The stream water samples had

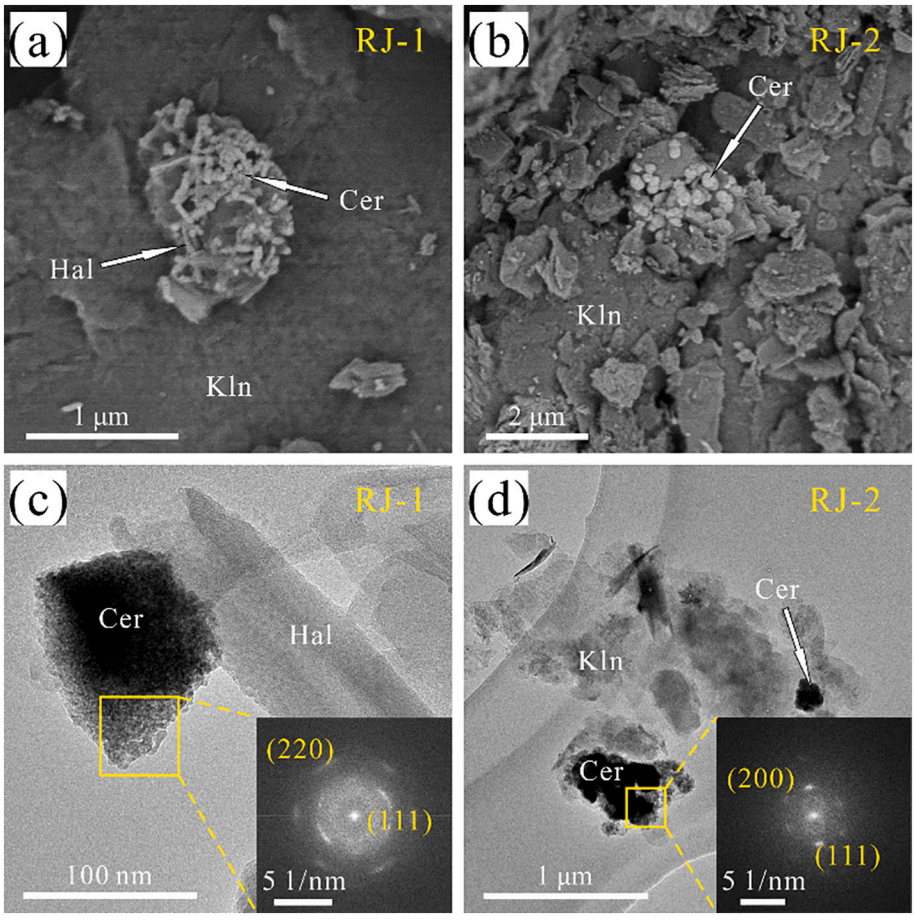

Fig. 5. (a, c) Scanning electron microscopy backscattered electron images and (b, d) transmission electron microscopy (TEM) images of cerianite in the A horizon of the Renju weathering crust. (a) Aggregates of granulate cerianite and tubular halloysite on the surface of laminar kaolinite layers. (b) High-resolution TEM (HRTEM) images of cerianite with fast Fourier transformations in the RJ-1 profile. (c) Globular cerianite aggregates attached to the surface of the laminar kaolinite layers. (d) HRTEM image of cerianite with fast Fourier transformations in the RJ-2 profile. Abbreviations: Cer = cerianite; Hal = halloysite; Kln = kaolinite.

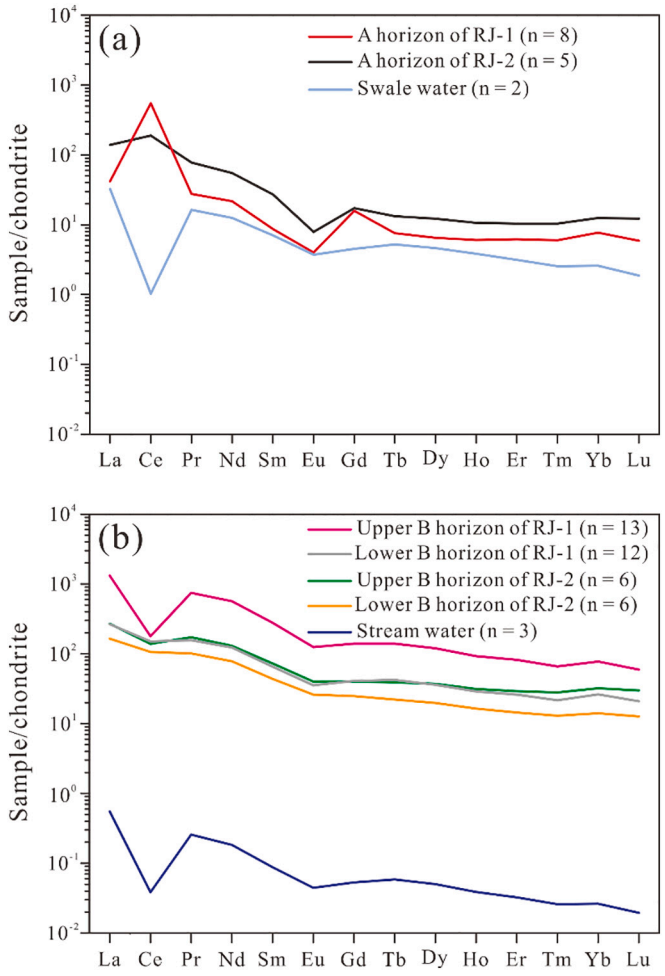

Fig. 6. Average chondrite-normalised rare earth element (REE) pattern for the different horizons and local groundwater (swale and stream water). Chondrite values are from McDonough and Sun (1995).

relatively low REE concentrations, ranging from 0.14 to 1.04 ppm (Fig. 6b). The chondrite-normalised patterns of the stream water samples are nearly identical to those of the swale water and B horizon in the Renju regolith profiles (Fig. 6a, b). The stream water samples exhibited relative LREE enrichment (LREE/HREE = 2.37–2.84), with a notably negative Ce anomaly (δCe = 0.10–0.11) and a slightly negative Eu anomaly (δEu = 0.63–0.73) (Fig. 6b).

5. Discussion

5.1. Proxies for groundwater table

Determination of the groundwater table is critical for constraining the redox environment and illuviation–eluviation dynamics related to REE mineralisation in the regolith of South China. Although the groundwater table can be obtained by borehole measurements (Jaunat et al., 2016), the late-stage development of geological structures (e.g., faults and joints) may have disrupted the previously formed stable hydrological system and altered the groundwater table of the investigated regolith (Gao et al., 2018; Long et al., 2019). Therefore, a prerequisite to unveiling the effects of groundwater on regolith-hosted REE deposits is to identify effective mineralogical and geochemical proxies that can be used to locate the groundwater table that developed during the formation of the investigated regolith and explore its coupling and fundamental relationship with the mineralisation of REEs.

Our study clearly shows the abrupt changes of Ce anomaly (Fig. 2), Fe-REE oxide colloids (Fig. 3), and mineral phase transition between goethite and hematite (Fig. 4) at a depth of ~10 m in the RJ-1 profile and ~ 5 m in the RJ-2 profile. These simultaneously occurring dramatic changes reflect significant variations in the hydrodynamic conditions and redox environments at the corresponding depth in the regolith (Zhukov and Bogatyrev, 2012; Öhlander et al., 2014; Navarre-Sitchler et al., 2015). The anomalies of redox-sensitive Ce should be ascribed to the distinct redox environments (Weng et al., 2019; Ichimura et al., 2020) while the abrupt change of the hematite/goethite phase components was resulted from the distinct hydrological environments above and below the groundwater table (Barrón and Torrent, 2013). Meanwhile, a fluctuation of oxic (unsaturated zone) and anoxic (saturated zone) environments is advantageous for Fe-REE oxides and kaolinite precipitation, respectively (Xiang and Banin, 1996; Han et al., 2001; Zhong et al., 2019). Thus, the depth with the above-mentioned abrupt changes most likely represents the location of the groundwater table. This is further verified by the water level of 3–6 m in a well on the investigated hillside (Fig. 1b, c).

5.1.1. Ce anomaly

Ce^{3+} is soluble in water and readily oxidises to Ce^{4+} under oxidising conditions (pH = 4–6, Eh > 1.0 V) (Bao and Zhao, 2008; Janots et al., 2015; Abellan et al., 2017). Ce is transported as Ce^{3+} in solution in a pathway similar to those of other LREEs under relatively reducing conditions (pH = 7, Eh < 0.8 V), whereas Ce^{4+} commonly precipitates as cerianite (CeO_2) in oxidising environments (Braun et al., 1990; Abellan et al., 2017; Ichimura et al., 2020). In the profiles of the Renju weathering crust, a boundary in the vicinity of the A horizon clearly divides positive and negative Ce anomalies (Fig. 2). The negative Ce anomaly in the swale water (Fig. 6) suggests that most of the Ce atoms released by the chemical weathering of REE-bearing minerals did not migrate in the water flow. Instead, the abundance of cerianite indicates that the released Ce tended to remain fixed via oxidation (Fig. 5). With the downward migration of other REEs, the gradual accumulation of cerianite resulted in positive and negative Ce anomalies above and below the boundary, respectively. This Ce anomaly boundary thus represents an interface that divides the oxic and anoxic environments in the regolith.

The saturated zone contains a steady low-permeability aquifer below the groundwater table. Atmospheric oxygen was expelled by ambient water in the pore spaces of the regolith (Zhukov and Bogatyrev, 2012; Kim et al., 2017; Arora et al., 2019). The saturated zone contains dissolved oxygen only with a low pO_2 of ~2×10^{-4} Pa (Abellan et al., 2017). In contrast, the vadose zone above the groundwater table has a high permeability and porosity with generally air-filled pores, which allow the ongoing replenishment of atmospheric oxygen (Holden and Fierer, 2005; Lachassagne et al., 2011). As a result, the vadose zone has significantly higher O_2 content with $pO_2 = 2.13 \times 10^4$–1.52×10^4 Pa (Holden and Fierer, 2005). The anomalies of redox-sensitive Ce (Weng et al., 2019; Ichimura et al., 2020) can likely be ascribed to the distinct redox environments above and below the groundwater table. The positive Ce anomalies are higher in the RJ-1 profile than in the RJ-2 profile (Fig. 2), indicating that RJ-1 on the ridge has a thicker vadose zone and larger head drop.

5.1.2. Fe-REE oxide colloids

The groundwater table is also responsible for the anomalies of other redox-sensitive major elements, such as Fe and Mn (Ma et al., 2007; Bazilevskaya et al., 2013), within a regolith profile. Horváth et al. (2000) interpreted the occurrence of Fe-oxide isopachous cement in a basalt weathering profile, as a direct indicator of an undulating groundwater table. Similar lamellar Fe-REE oxide cement was observed on kaolinite slag in the vicinity of the inferred groundwater table in the Renju regolith (Fig. 3). The favourable environments for Fe-REE oxides and kaolinite precipitation correspond to an oxic unsaturated zone and anoxic saturated zone, respectively (Xiang and Banin, 1996; Han et al.,

2001; Zhong et al., 2019). In South China, the alternation of rainy and dry seasons can cause fluctuations of the groundwater table over a range of several meters (Yang et al., 2015). Thus, the alternating patterns of lamellar Fe-REE oxide colloids are considered to be related to the undulating hydrological environment in the vicinity of the groundwater table in the regolith.

5.1.3. Variations of goethite and hematite contents in the profiles

During the primary weathering stage, Fe released from primary minerals (e.g. biotite and magnetite) tends to form nanocrystalline ferrihydrite ($Fe_{10}O_{14}(OH)_2{\cdot}nH_2O$) (Cornell and Schwertmann, 2003; Barrón and Torrent, 2013). However, this molecule is meta-stable and readily transforms into different and more thermodynamically stable Fe-(hydr)oxides, corresponding to the specific physicochemical conditions of the ambient environment (Fig. 3). For example, ferrihydrite transforms to goethite (α-FeOOH) in a humid environment, and into hematite (α-Fe_2O_3) in an oxic and dry environment (Horváth et al., 2000; Cornell and Schwertmann, 2003; Barrón and Torrent, 2013). In the Renju weathering profiles, a dramatic change in the proportions of hematite and goethite occurs at the Ce anomaly boundary. Hematite is a dominant Fe-(hydr)oxide phase above the boundary, whereas the proportion of goethite abruptly increases below the boundary (Fig. 4). The abrupt change in the hematite/goethite ratio in the regolith profile is likely related to the distinct hydrological environments above and below the groundwater table.

5.2. Vertical eluviation of REEs in the vadose zone

The meteoric water in South China is weakly acidic (Huo et al., 2010; Sun et al., 2010) and tends to become increasingly acidic and corrosive due to acidification by humic acids in the topsoil (Bao and Zhao, 2008). The results of swale water analyses suggest that the pH values of the meteoric water that percolates through the humus-rich topsoil layer generally range from 5.12 to 6.14 (Appendix Table A.8). This relatively acidic water facilitates the release of REEs by dissolving REE-bearing minerals. The relatively high ΣREE content (32.4–37.2 ppm) in the swale water suggests that the acidic water percolating into the vadose zone can act as a leaching fluid that activates REE ions and complexes temporarily fixed by supergene minerals (Biddau et al., 2002; Pourret et al., 2007; Li et al., 2017a).

The vadose zone in the Renju regolith is generally composed of 40–70% supergene minerals, 30–60% quartz and K-feldspar, and exhibits a loose architecture with high porosity (Fig. 2). The highly permeable vadose zone facilitates migration of REEs with water flow (Wyns et al., 2004; Navarre-Sitchler et al., 2009; Jaunat et al., 2016). The air-filled pores can be transiently filled with seepage water, and is subsequently drained with the water flowing downwards (Holden and Fierer, 2005; Niswonger et al., 2006). The sequential extraction analyses reveal that the ΣREE budget in the vadose zone is mainly controlled by the residual fraction, and the ion exchangeable fraction only accounts for 12.3–31.0 wt% (Fig. 2). The low iREE content suggests that the seepage water can effectively leach REE ions in the vadose zone and transport them downwards to deeper parts of the regolith, especially when the seepage water is sustainably replenished by rainwater during the rainy season (Wyns et al., 2004; Jaunat et al., 2016). Vertical eluviation thus provides a continuous force driving the downward migration of REE ions in the vadose zone of the regolith in South China.

5.3. REE mineralisation in the saturated zone

Previous studies have suggested that REE mineralisation in regolith is controlled by the type, content, and surface reactivity of supergene clay minerals (Sanematsu and Watanabe, 2016; Li et al., 2017b; Li and Zhou, 2020). Experimental modelling has demonstrated that the REE adsorption capabilities of kaolinite and halloysite are enhanced with increasing pH (Coppin et al., 2002; Yang et al., 2019). At pH = 5, the REE adsorption capacities of kaolinite and halloysite can reach 1.61×10^3 and 3.46×10^3 ppm, respectively (Yang et al., 2019), which are generally larger than the iREE contents in the Renju regolith (Fig. 2).

In the Renju regolith, the kaolinite and halloysite contents gradually increase to 38–65% and 3–16% in the upper B horizon, respectively (Fig. 2). Moreover, the pH values of the weathering crust gradually increase from the upper A horizon to the B horizon (Fig. 2) due to the ongoing consumption of H^+ during the dissolution of primary minerals, which facilitates the adsorption of REEs by clay minerals (Li et al., 2017b). The iREEs in the RJ-1 and RJ-2 profiles are intensively concentrated at depths of 5–15 m and 10–32 m below the inferred groundwater table, respectively, accounting for more than 66.5% and 59.4% of the bulk REE budget (Fig. 2). The gradual variations of the clay mineral type and content and pH values along the profile (Fig. 2) are incongruent with the abrupt enrichment of REEs below the groundwater table.

The spatial coincidence between the iREE concentrated zone and the inferred groundwater table suggests that REE ions that are leached downwards from the vadose zone are adsorbed by clay minerals in the saturated zone in the vicinity of the groundwater table. In the saturated zone, the seepage driving force transforms from gravitational potential to pressure potential (Tóth, 1999; Tóth et al., 2016), and the lateral flow dominates the migration of iREEs. The equivalent porous media model (Jaunat et al., 2016) suggests that the permeability of the saturated zone is two orders of magnitude lower than that of the vadose zone. The groundwater table can thus act as a physical hindrance that dramatically reduces the fluidity of the water flow (Zhukov and Bogatyrev, 2012; Tóth et al., 2016). The low permeability of the saturated zone results in slow compositional renewal of the groundwater, which commonly take one to several years (Tóth et al., 2016; Arora et al., 2019). The low water flow rate in the saturated zone is thus advantageous for the adsorption of most iREE ions by kaolinite and other secondary minerals, which can reach equilibrium within several days (Yang et al., 2019). The low REE contents (ΣREE = 0.14–1.04 ppm) of the stream water (Fig. 6b) demonstrate that REEs can be largely adsorbed in the saturated zone, which facilitates the formation of REE deposits in regolith.

5.4. Genetic model

The low hill landforms, subtropical climate, and sufficient rainfall in the Renju mining area are beneficial for the formation of thick regolith (locally up to 86 m) (Fig. 7a). The groundwater system in the regolith includes a vadose zone above the groundwater table and a saturated zone below the groundwater table. The vadose zone is highly porous and permeable. When continuously replenished by rainfall, meteoritic water continuously leaches REEs in the regolith, which migrate downwards with vertical flow in the vadose zone. In contrast, the saturated zone has a relatively steady aquifer with low permeability, resulting in the adsorption of REEs by kaolinite and halloysite and a relatively low REE concentration in the stream water. The persistent eluviation–illuviation processes provide a driving force for the continuous downward migration of REEs, resulting in the accumulation of REEs below the groundwater table and the formation of lenticular-shaped REE ore bodies in the vicinity of the groundwater table in the regolith (Fig. 7b).

6. Conclusions

Systematic geochemical and mineralogical investigations of the profiles from the Renju REE deposit demonstrate that an abrupt change in the Ce anomaly, the occurrence of Fe-REE oxide colloids, and prominent variations of the goethite and hematite phases are effective indicators that can be used to determine the groundwater table in regolith. The groundwater table plays a key role in the formation of regolith-hosted REE deposits in South China. The iREEs released from the weathering of REE-bearing minerals readily migrate downwards with leaching fluids in the vadose zone above the groundwater table.

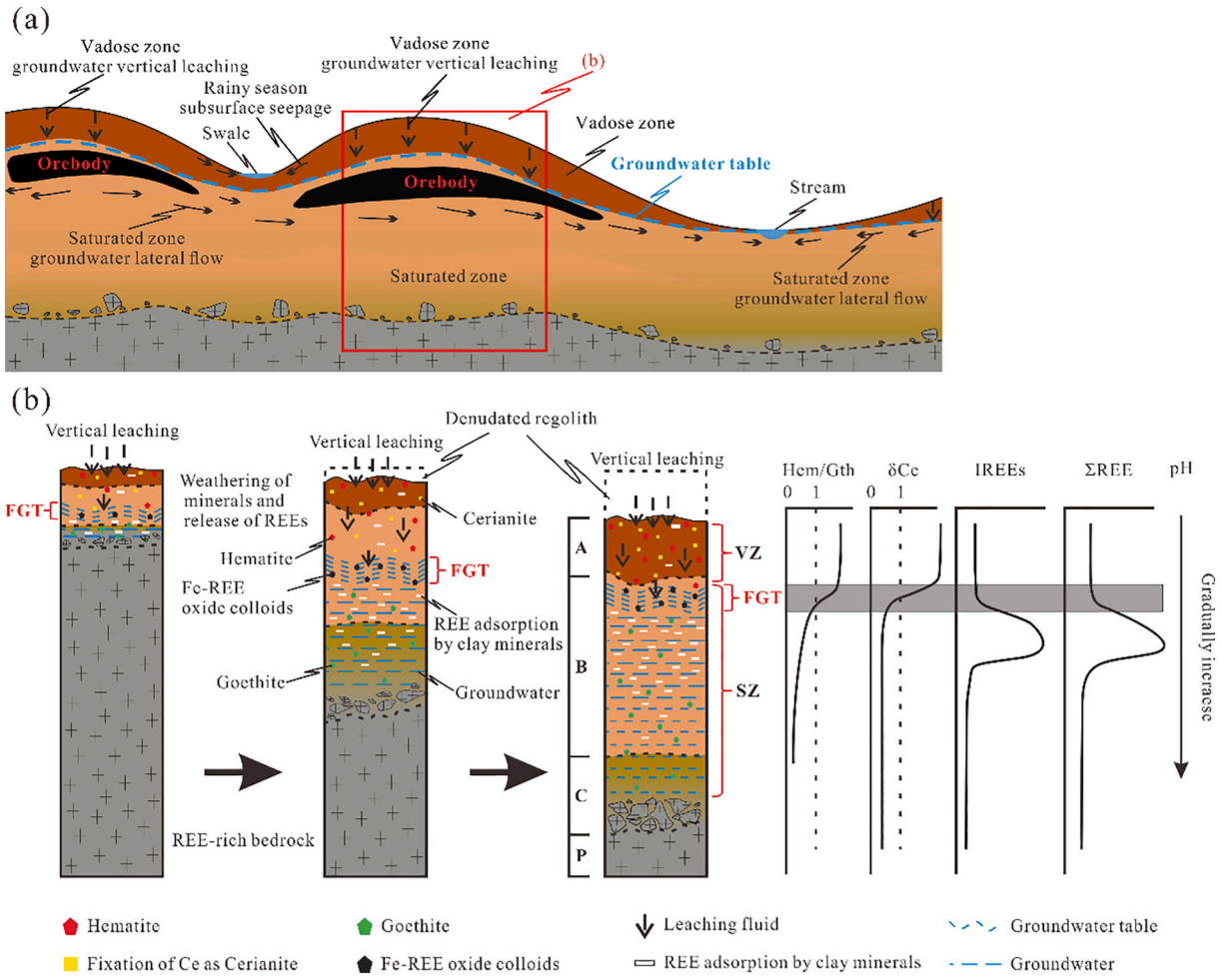

Fig. 7. (a) Dominant factors controlling rare earth element (REE) mobilisation and redistribution, and distribution of REE ore bodies in a weathered catchment. (b) Schematic model illustrating the formation of the Renju regolith-hosted REE deposit. Abbreviations: Hem = hematite; Gth = goethite; δCe = Ce anomalies; IREEs = ion-exchangeable rare earth elements; ΣREE = total rare earth elements; Fgt = fluctuation zone of the groundwater table; VZ = vadose zone (leached zone); SZ = saturated zone.

However, the relatively low permeability of the saturated zone below the groundwater table strongly facilitates the adsorption of REE ions by clay minerals and other secondary minerals. A long-term eluviation–illuviation process leads to the continuous accumulation of iREEs in the saturated zone to form lenticular-shaped REE ore bodies.

In South China, the locations of REE fertile zones in regolith-hosted REE deposits have been observed at different depths in the investigated profiles (Sanematsu and Watanabe, 2016; Li et al., 2017b). Previous studies ascribed the spatial variations of the REE fertile zones to the factors such as weathering intensity, denudation rate, and pH variations in different regolith (Bao and Zhao, 2008; Sanematsu and Watanabe, 2016; Li et al., 2020). The results of this study suggest that the location of an REE fertile zone is essentially controlled by the groundwater table that formed synchronously with the regolith and REE mineralisation. The original hydrological systems and location of the REE fertile zone can be altered by post-mineralisation tectonic activity and denudation. The observed distributions of the REE fertile zones correspond to the contemporary groundwater table during the formation of regolith-hosted REE deposits. These findings provide insights on the spatial variations of REE fertile zones in different REE deposits.

Declaration of Competing Interest

The authors declare that they have no known competing financial interests or personal relationships that could have appeared to influence the work reported in this paper.

Acknowledgements

This work was financially supported by the National Key R&D Programme of China (Grant No. 2017YFC0602306); supported by the Key Research Program of the Institute of Geology & Geophysics, CAS (Grant No. IGGCAS-201901); the National Natural Science Foundation of China (Grant Nos. 41921003 and 41773113); Science Research Program of Guangzhou, China (Grant No. 201804020037); and Science and Technology Planning of Guangdong Province, China (Grant Nos. 2017B030314175, 2020B1212060055, 2020B1515020015 and 2017GC010578). This is contribution No.IS-3015 from GIGCAS.

Appendix A. Supplementary data

Supplementary data to this article can be found online at https://doi.org/10.1016/j.chemgeo.2021.120295.

References

Abellan, P., Moser, T.H., Lucas, I.T., Grate, J.W., Evans, J.E., Browning, N.D., 2017. The formation of cerium(III) hydroxide nanoparticles by a radiation mediated increase in local pH. RSC Adv. 7, 3831–3837.
Alakangas, L.J., Mathurin, F.A., Astrom, M.E., 2020. Diverse fractionation patterns of rare earth elements in deep fracture groundwater in the baltic shield - progress from

utilisation of Diffusive Gradients in Thin-films (DGT) at the Aspo Hard Rock Laboratory. Geochim. Cosmochim. Ac 269, 15–38.
Arora, B., Dwivedi, D., Faybishenko, B., Jana, R.B., Wainwright, H.M., 2019. Understanding and predicting vadose zone processes. Rev. Mineral. Geochem. 85, 303–328.
Aubert, D., Stille, P., Probst, A., 2001. REE fractionation during granite weathering and removal by waters and suspended loads: Sr and Nd isotopic evidence. Geochim. Cosmochim. Ac 65, 387–406.
Bao, Z.W., Zhao, Z.H., 2008. Geochemistry of mineralization with exchangeable REY in the weathering crusts of granitic rocks in South China. Ore Geol. Rev. 33, 519–535.
Barrón, V., Torrent, J., 2013. Iron, manganese and aluminium oxides and oxyhydroxides. Emu Notes Mineral. 14, 297–336.
Bazilevskaya, E., Lebedeva, M., Pavich, M., Rother, G., Parkinson, D.Y., Cole, D., Brantley, S.L., 2013. Where fast weathering creates thin regolith and slow weathering creates thick regolith. Earth Surf. Process. Landf. 38, 847–858.
Berger, A., Janots, E., Gnos, E., Frei, R., Bernier, F., 2014. Rare earth element mineralogy and geochemistry in a laterite profile from Madagascar. Appl. Geochem. 41, 218–228.
Biddau, R., Cidu, R., Frau, F., 2002. Rare earth elements in waters from the albitite-bearing granodiorites of Central Sardinia, Italy. Chem. Geol. 182, 1–14.
Borst, A.M., Smith, M.P., Finch, A.A., Estrade, G., Villanova-de-Benavent, C., Nason, P., Marquis, E., Horsburgh, N.J., Goodenough, K.M., Xu, C., Kynicky, J., Geraki, K., 2020. Adsorption of rare earth elements in regolith-hosted clay deposits. Nat. Commun. 11, 1–15.
Braun, J.J., Pagel, M., Muller, J.P., Bilong, P., Michard, A., Guillet, B., 1990. Cerium anomalies in lateritic profiles. Geochim. Cosmochim. Ac 54, 781–795.
Braun, J.J., Riotte, J., Battacharya, S., Violette, A., Oliva, P., Prunier, J., Marechal, J.C., Ruiz, L., Audry, S., Subramanian, S., 2018. REY-Th-U Dynamics in the critical zone: combined influence of reactive bedrock accessory minerals, authigenic phases, and hydrological sorting (Mule Hole Watershed, South India). Geochem. Geophys. Geosyst. 19, 1611–1635.
Bray, A.W., Oelkers, E.H., Bonneville, S., Wolff-Boenisch, D., Potts, N.J., Fones, G., Benning, L.G., 2015. The effect of pH, grain size, and organic ligands on biotite weathering rates. Geochim. Cosmochim. Ac 164, 127–145.
Chen, B.H., Yu, S.J., 1994. The geological and geochemical characteristics of late Yanshanian granites in Renju-Huangshe area, Pingyuan, Guangdong. Acta Sci. Nat. Univ. Sunyatseni 33, 130–133 (in Chinese with English abstract).
Chen, B.H., Yu, S.J., 1995. The weathering crust and REE metallogenic characteristics of granite in Pingyuan, Guangdong. Acta Sci. Nat. Univ. Sunyatseni 34, 96–101 (in Chinese with English abstract).
Coppin, F., Berger, G., Bauer, A., Castet, S., Loubet, M., 2002. Sorption of lanthanides on smectite and kaolinite. Chem. Geol. 182, 57–68.
Cornell, R.M., Schwertmann, U., 2003. The Iron Oxides: Structure, Properties, Reactions, Occurences and Uses. Wiley-VCH.
Cudahy, T.J., Ramanaidou, E.R., 1997. Measurement of the hematite:goethite ratio using field visible and near-infrared reflectance spectrometry in channel iron deposits, western Australia. Aust. J. Earth Sci. 44, 411–420.
Denys, A., Janots, E., Auzende, A.L., Lanson, M., Findling, N., Trcera, N., 2021. Evaluation of selectivity of sequential extraction procedure applied to REE speciation in laterite. Chem. Geol. 559.
Duzgoren-Aydin, N.S., Aydin, A., 2009. Distribution of rare earth elements and oxyhydroxide phases within a weathered felsic igneous profile in Hong Kong. J. Asian Earth Sci. 34, 1–9.
Fu, W., Li, X.T., Feng, Y.Y., Feng, M., Peng, Z., Yu, H.X., Lin, H.R., 2019. Chemical weathering of S-type granite and formation of rare earth element (REE)-rich regolith in South China: critical control of lithology. Chem. Geol. 520, 33–51.
Gao, Q., Shang, Y.J., Hasan, M., Jin, W.J., Yang, P., 2018. Evaluation of a weathered rock aquifer using ERT method in South Guangdong, China. Water 10, 1–22.
Gleeson, T., Befus, K.M., Jasechko, S., Luijendijk, E., Cardenas, M.B., 2016. The global volume and distribution of modern groundwater. Nat. Geosci. 9, 161–171.
Han, F.X., Banin, A., Triplett, G.B., 2001. Redistribution of heavy metals in arid-zone soils under a wetting-drying cycle soil moisture regime. Soil Sci. 166, 18–28.
Holden, P.A., Fierer, N., 2005. Microbial processes in the vadose zone. Vadose Zone J. 4, 1–21.
Horváth, Z., Varga, B., Mindszenty, A., 2000. Micromorphological and chemical complexities of a lateritic profile from basalt (Jos Plateau, Central Nigeria). Chem. Geol. 170, 81–93.
Huo, M.Q., Sun, Q., Bai, Y.H., Xie, P., Liu, Z.R., Li, J.L., Wang, X.S., Lu, S.H., 2010. Chemical character of precipitation and related particles and trace gases in the North and South of China. J. Atmos. Chem. 67, 29–43.
Ichimura, K., Sanematsu, K., Kon, Y., Takagi, T., Murakami, T., 2020. REE redistributions during granite weathering: Implications for Ce anomaly as a proxy for paleoredox states. Am. Mineral. 105, 848–859.
Janots, E., Bernier, F., Brunet, F., Munoz, M., Trcera, N., Berger, A., Lanson, M., 2015. Ce (III) and Ce(IV) (re)distribution and fractionation in a laterite profile from Madagascar: insights from in situ XANES spectroscopy at the Ce L-III-edge. Geochim. Cosmochim. Ac 153, 134–148.
Jaunat, J., Dupuy, A., Huneau, F., Celle-Jeanton, H., Le Coustumer, P., 2016. Groundwater flow dynamics of weathered hard-rock aquifers under climate-change conditions: an illustrative example of numerical modeling through the equivalent porous media approach in the North-Western Pyrenees (France). Hydrogeol. J. 24, 1359–1373.
Kim, H., Stinchcomb, G., Brantley, S.L., 2017. Feedbacks among O_2 and CO_2 in deep soil gas, oxidation of ferrous minerals, and fractures: a hypothesis for steady-state regolith thickness. Earth Planet Sc Lett. 460, 29–40.
Kimberley, M.M., Abu-Jaber, N., 2005. Shallow perched groundwater, a flux of deep CO_2, and near-surface water–rock interaction in Northeastern Jordan: an example of positive feedback and Darwin's "warm little pond". Precambrian Res. 137, 273–280.
King, E.K., Pett-Ridge, J.C., 2018. Reassessing the dissolved molybdenum isotopic composition of ocean inputs: the effect of chemical weathering and groundwater. Geology 46, 955–958.
Lachassagne, P., Wyns, R., Dewandel, B., 2011. The fracture permeability of hard rock aquifers is due neither to tectonics, nor to unloading, but to weathering processes. Terra Nova 23, 145–161.
Li, M.Y.H., Zhou, M.F., 2020. The role of clay minerals in formation of the regolith-hosted heavy rare earth element deposits. Am. Mineral. 105, 92–108.
Li, M.X., Liu, H.B., Chen, T.H., Hayat, T., Alharbi, N.S., Chen, C.L., 2017a. Adsorption of Europium on Al-substituted goethite. J. Mol. Liq. 236, 445–451.
Li, Y.H.M., Zhao, W.W., Zhou, M.F., 2017b. Nature of parent rocks, mineralization styles and ore genesis of regolithhosted REE deposits in South China: an integrated genetic model. J. Asian Earth Sci. 148, 65–95.
Li, M.Y.H., Zhou, M.F., Williams-Jones, A.E., 2019. The genesis of regolith-hosted heavy rare earth element deposits: insights from the world-class Zudong deposit in Jiangxi Province, South China. Econ. Geol. 114, 541–568.
Li, M.Y.H., Zhou, M.F., Williams-Jones, A.E., 2020. Controls on the dynamics of rare earth elements during subtropical hillslope processes and formation of regolith-hosted deposits. Econ. Geol. 115, 1097–1118.
Long, X.T., Zhang, K.N., Yuan, R.Q., Zhang, L., Liu, Z.L., 2019. Hydrogeochemical and isotopic constraints on the pattern of a deep circulation groundwater flow system. Energies 12, 1–18.
Ma, J.L., Wei, G.J., Xu, Y.G., Long, W.G., Sun, W.D., 2007. Mobilization and re-distribution of major and trace elements during extreme weathering of basalt in Hainan Island, South China. Geochim. Cosmochim. Ac 71, 3223–3237.
Mcdonough, W.F., Sun, S.S., 1995. The composition of the earth. Chem. Geol. 120, 223–253.
Navarre-Sitchler, A., Steefel, C.I., Yang, L., Tomutsa, L., Brantley, S.L., 2009. Evolution of porosity and diffusivity associated with chemical weathering of a basalt clast. J. Geophys. Res-Earth 114, 1–14.
Navarre-Sitchler, A., Brantley, S.L., Rother, G., 2015. How porosity increases during incipient weathering of crystalline silicate rocks. Rev. Mineral. Geochem. 80, 331–354.
Nesbitt, H.W., Young, G.M., 1982. Early Proterozoic climates and plate motions inferred from major element chemistry of lutites. Nature 299, 715–717.
Niswonger, R.G., Prudic, D.E., Regan, R.S., 2006. Documentation of the Unsaturated-Zone Flow (UZF1) Package for Modeling Unsaturated Flow between the Land Surface and the Water Table with MODFLOW-2005: U.S. Geological Survey Techniques and Methods 6-A19 (62 p).
Öhlander, B., Land, M., Ingri, J., Widerlund, A., 2014. Mobility and transport of Nd isotopes in the vadose zone during weathering of granitic till in a boreal forest. Aquat. Geochem. 20, 1–17.
Pourret, O., Davranche, M., Gruau, G., Dia, A., 2007. Competition between humic acid and carbonates for rare earth elements complexation. J. Colloid Interface Sci. 305, 25–31.
Rasmussen, C., Brantley, S., Richter, D.D., Blum, A., Dixon, J., White, A.F., 2011. Strong climate and tectonic control on plagioclase weathering in granitic terrain. Earth Planet Sc Lett. 301, 521–530.
Regional Geological Survey Team of Jiangxi Geological Burea, 1976. Report of 1:200,000 Regional Geological Survey of the Xunwu Region: Anyuan, 56 (in Chinese).
Riesgo García, M.V., Krzemień, A., Manzanedo del Campo, M.Á., Menéndez, Álvarez M., Richard, Gent M., 2017. Rare earth elements mining investment: it is not all about China. Res. Policy 53, 66–76.
Salve, R., Rempe, D.M., Dietrich, W.E., 2012. Rain, rock moisture dynamics, and the rapid response of perched groundwater in weathered, fractured argillite underlying a steep hillslope. Water Resour. Res. 48, 1–25.
Sanematsu, K., Watanabe, Y., 2016. Characteristics and genesis of ion-adsorption type deposits. Rev. Econ. Geol. 18, 55–79.
Shi, C., Yan, M., Liu, C., Chi, Q., Hu, S., Gu, T., Bo, W., Yan, W., 2005. Abundances of chemical elements in granitoids of China and their characteristics. Geochimica 34, 470–482.
Sun, M.H., Wang, Y., Wang, T., Fan, S.J., Wang, W.X., Li, P.H., Guo, J., Li, Y.H., 2010. Cloud and the corresponding precipitation chemistry in South China: Water-soluble components and pollution transport. J. Geophys. Res.-Atmos. 115, 1–10.
Tang, J.W., Johannesson, K.H., 2010. Ligand extraction of rare earth elements from aquifer sediments: implications for rare earth element complexation with organic matter in natural waters. Geochim. Cosmochim. Ac 74, 6690–6705.
Taunton, A.E., Welch, S.A., Banfield, J.F., 2000. Microbial controls on phosphate and lanthanide distributions during granite weathering and soil formation. Chem. Geol. 169, 371–382.
Tóth, J., 1999. Groundwater as a geologic agent: an overview of the causes, processes, and manifestations. Hydrogeol. J. 7, 1–14.
Tóth, Á., Havril, T., Simon, S., Galsa, A., Santos, F.A.M., Müller, I., Mádl-Szonyi, J., 2016. Groundwater flow pattern and related environmental phenomena in complex geologic setting based on integrated model construction. J. Hydrol. 539, 330–344.
Wallrich, I.L.R., Stewart, B.W., Capo, R.C., Hedin, B.C., Phan, T.T., 2020. Neodymium isotopes track sources of rare earth elements in acidic mine waters. Geochim. Cosmochim. Ac 269, 465–483.
Wang, Z.G., Xu, J.H., 2016. Characteristics and prevention measures of soil erosion in Renju rare earth mining area in northern Guangdong province. Subtrop. Soil Water Conserv. 28, 51–56 (in Chinese).

Wang, J.L., Jin, M.G., Lu, G.P., Zhang, D., Kang, F.X., Jia, B.J., 2016. Investigation of discharge-area groundwaters for recharge source characterization on different scales: the case of Jinan in northern China. Hydrogeol. J. 24, 1723–1737.
Weng, S.F., Yu, W.C., Algeo, T.J., Du, Y.S., Li, P.G., Lei, Z.Y., Zhao, S., 2019. Giant bauxite deposits of South China: multistage formation linked to Late Paleozoic Ice Age (LPIA) eustatic fluctuations. Ore Geol. Rev. 104, 1–13.
Wyns, R., Baltassat, J.M., Lachassagne, P., Legchenko, A., Vairon, J., Mathieu, F., 2004. Application of proton magnetic resonance soundings to groundwater reserve mapping in weathered basement rocks (Brittany, France). B Soc. Geol. Fr 175, 21–34.
Xiang, H.F., Banin, A., 1996. Solid-phase manganese fractionation changes in saturated arid-zone soils: pathways and kinetics. Soil Sci. Soc. Am. J. 60, 1072–1080.
Yang, Q., Hou, Z., Wang, Y., Zhao, Y., Delgado, J., 2015. A comparative study of shallow groundwater level simulation with WA-ANN and ITS model in a coastal island of South China. Arab. J. Geosci. 8, 6583–6593.
Yang, M.J., Liang, X.L., Ma, L.Y., Huang, J., He, H.P., Zhu, J.X., 2019. Adsorption of REEs on kaolinite and halloysite: a link to the REE distribution on clays in the weathering crust of granite. Chem. Geol. 525, 210–217.
Yu, C.X., Drake, H., Mathurin, F.A., Astrom, M.E., 2017. Cerium sequestration and accumulation in fractured crystalline bedrock: the role of Mn-Fe (hydr-)oxides and clay minerals. Geochim. Cosmochim. Ac 199, 370–389.
Zhao, L.L., Hong, H.L., Liu, J.C., Fang, Q., Yao, Y.Z., Tan, W., Yin, K., Wang, C.W., Chen, M., Algeo, T.J., 2018. Assessing the utility of visible-to-shortwave infrared reflectance spectroscopy for analysis of soil weathering intensity and paleoclimate reconstruction. Palaeogeogr. Palaeocl. 512, 80–94.
Zhong, Y., Liu, Q.S., Chen, Z., Gonzalez, F.J., Hein, J.R., Zhang, J., Zhong, L.F., 2019. Tectonic and paleoceanographic conditions during the formation of ferromanganese nodules from the northern South China Sea based on the high-resolution geochemistry, mineralogy and isotopes. Mar. Geol. 410, 146–163.
Zhukov, V.V., Bogatyrev, B.A., 2012. Dynamic models of lateritic bauxite formation. Geol. Ore Deposit. 54, 370–397.